3P3W Grid-Connected Hybrid-Frequency Parallel Inverter System With Wireless Synchronization

Tsai-Fu Wu, *Senior Member, IEEE*, Temir Sakavov, *Member, IEEE*,
Chien-Chih Hung, *Graduate Student Member, IEEE*, and Jui-Yang Chiu, *Graduate Student Member, IEEE*

***Abstract*—In this article, an extension of the hybrid-frequency parallel inverter system (HbFPIS) belonging to wide-bandgap/silicon (WBG/Si) hybrid family is discussed. HbFPIS contains two inverters connected in parallel, each having a specific function. The low-frequency high-power inverter's primary function is to achieve high power output with low-frequency modulation. The high-frequency low-power inverter, having a high dynamic response, is used to improve output current quality by ripple attenuation. In this article, three-phase three-wire (3P3W) HbFPIS topology is designed and implemented. The ripple compensation in 3P3W HbFPIS topology involves ripple models presented in this article. A wireless carrier synchronization algorithm based on ripple modeling is implemented, resulting in autonomy and increased reliability of the parallel modules. Simulated and experimental results from 20-kVA grid-connected 3P3W HbFPIS have confirmed the analysis and discussion.**

***Index Terms*—Control synchronization, direct digital control, division–summation (D–Σ) process, grid connection, hybrid-frequency parallel converters, three-phase three-wire (3P3W) inverters.**

I. Introduction

THREE-PHASE three-wire (3P3W) converters are commonly used in dc microgrids, electrical traction systems, flywheel energy dispatching applications, etc. Passive filters are used to improve the output currents of such converters, suppressing grid and pulse width modulation (PWM)-induced harmonics [1]. Single inverter systems are simple but rigid in optimization and are a less reliable solution. Modular parallel inverter systems allow for flexible optimization of cost/functionality with added reliability [2]. Parallel inverters are known to have circulation problems investigated in [3]. However, hybrid-frequency parallel inverter systems (HbFPIS) employ circulation to attenuate PWM-induced harmonics and improve output current quality. HbFPIS belongs to wide-bandgap/silicon (WBG/Si) hybrid family [4], [5], [6]. Such a structure allows for flexibility of cost/functionality tradeoffs. The optimization techniques for such hybrid systems were presented in [4], [7], and [8]. The attempt to apply HbFPIS in 3P3W with a common dc bus was discussed in [9]. The so-called virtual "fourth wire" effect leads to identical to the 3P4W HbFPIS design and ripple attenuation algorithms. To widen the WBG/Si hybrid family, 3P3W HbFPIS with separate dc sources as in Fig. 1 is implemented in this article. Due to the circulation path through a common source disconnected, both modules are topologically 3P3W. This needs the implementation of a different ripple model for ripple attenuation. Design differences between the proposed and existing topologies will be discussed. The inductor current ripple modeling for 3P3W topology was presented in [10] and [11]. These models are used for dc link ripple prediction [12], in variable frequency control [13]. In this article, the 3P3W ripple model is utilized for ripple attenuation and wireless synchronization.

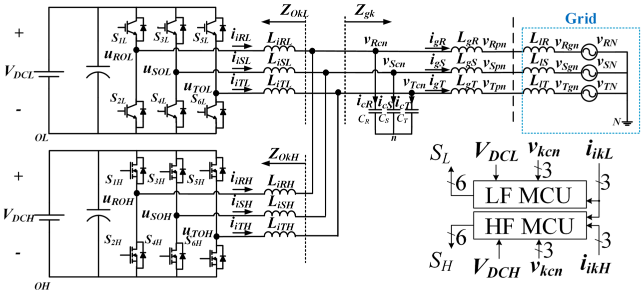

Fig. 1. 3P3W HbFPIS with separate DC voltage supplies.

If module controllers are implemented on independent microcontrollers [6], program sequences would require carrier synchronization to achieve ripple attenuation. Wired communication in primary/secondary architecture would compromise the reliability of a parallel system. To avoid the loss of reliability, a wireless synchronization technique should be applied. One way to wirelessly synchronize parallel inverters is to use virtual oscillator control [14], [15]. Although this approach is applicable for inverters operating at the same frequency, it is not applicable for carrier-level synchronization. Carrier synchronization was investigated in [16], but this work still requires primary/secondary architecture. Wireless communication methods [17], [18] require the usage of radio transmission modules and still require primary/secondary architecture. Proposed wireless synchronization uses modeled and measured ripple comparison. An additional Hall sensor in a high-frequency low-power

Manuscript received 13 April 2023; revised 18 July 2023; accepted 27 August 2023. Date of publication 4 September 2023; date of current version 23 October 2023. This work was supported by the Ministry of Science and Technology, Taiwan. Recommended for publication by Associate Editor S.K.M. *(Corresponding author: Tsai-Fu Wu.)*

The authors are with the Department of Electrical Engineering, National Tsing Hua University, Hsinchu 30013, Taiwan (e-mail: tfwu@ee.nthu.edu.tw; temirsakau@gmail.com; s110061801@m110.nthu.edu.tw; s110061802@m110.nthu.edu.tw).

Color versions of one or more figures in this article are available at https://doi.org/10.1109/TPEL.2023.3311401.

Digital Object Identifier 10.1109/TPEL.2023.3311401

inverter (HFLPI) is connected to measure the inductance current in the low-frequency high-power inverter (LFHPI) module.

Cross-correlation or convolution is widely used in a variety of fields, such as image processing and pattern matching [19], [20]. Convolutional neural networks are used in many image classification algorithms [21]. Considering the limitations, pattern matching-based synchronization will utilize simple convolution as a metric of similarity.

To introduce the design of a novel 3P3W HbFPIS with wireless synchronization, the article is structured as follows. In Section II, the inverter-side inductor current ripple models are compiled. These models are used for online simulation and ripple attenuation in HbFPIS. The connection between 3 W and 4 W models is briefly discussed. In Section III, a wireless synchronization algorithm based on online ripple simulation is proposed. In Section IV, the direct digital control of LFHPI and HFLPI for 3P3W topology is presented. The feasibility of ripple attenuation in 3P3W HbFPIS topology is discussed. In Section V, an indirect comparison of ripple attenuation ratios for 4 W and 3 W is performed. Based on these comparisons, design considerations are made. In Section VI, the current tracking capability and overall stability of the 3P3W HbFPIS are analyzed. Section VII includes simulated and experimental results of 20-kVA 3P3W HbFPIS and the results of the study are concluded in Section VIII.

II. INVERTER-SIDE INDUCTANCE CURRENT RIPPLE MODELS

To attenuate the current ripple generated by LFHPI, the controller of HFLPI conducts an online simulation according to the model of ripple and forms the reference $i_{rpk}[n+1]$ based on this simulation.

A. 3P3W Inverter-Side Inductor Current Ripple Model

In the 3P3W ripple model, the voltage vector V_i is defined as a binary number with three fixed positions $V_i = [sw_R, sw_S, sw_T]$ where $s\,w_k = 0$ meaning that the upper switch of phase k is the nonconducting and the lower switch of phase k is conducting and $s\,w_k = 1$ is the opposite.

3P3W inductor current ripple model for the next switching cycle n+1 can be represented in the time domain as

$$i_{ik.3\mathrm{W}}\ (t) = \begin{cases} \alpha_{V_7 k}\,[n+1]\cdot(t-t_0)\,, & t_0 \le t \le t_1 \\ i_{ik3\mathrm{W}}\,(t_1) + \alpha_{V_x k}\,[n+1]\cdot(t-t_1)\,, & t_1 < t \le t_2 \\ i_{ik3\mathrm{W}}\,(t_2) + \alpha_{V_y k}\,[n+1]\cdot(t-t_2)\,, & t_2 < t \le t_3 \\ i_{ik3\mathrm{W}}\,(t_3) + \alpha_{V_0 k}\,[n+1]\cdot(t-t_3)\,, & t_3 < t \le \frac{T_L}{2} \\ -i_{ik.3\mathrm{W}}\,(T_{sL}-t)\,, & \frac{T_{sL}}{2} < t \le T_{sL} \end{cases}$$

$$x, y\ = \{1, 2, \ldots, 6\}\ ,\ x \ne y. \tag{1}$$

where $t_0 = 0$ and the time moments t_1, t_2, and t_3 are sorted from earlier to latest from the group $\{t_R, t_S,\ t_T\}$,.which is calculated as

$$t_k = \frac{T_{sL}\,(1 - D^*_{kL}\,[n+1])}{2}\ ,\quad k\ = \{R, S, T\}\ . \tag{2}$$

TABLE I
VOLTAGE VECTORS AND MOMENTS OF SWITCHING BETWEEN THEM VERSUS SORTED ESTIMATED DUTIES

Relation of estimated duties in LFHPI	t_1	t_2	t_3	V_x $t \in (t_1, t_2]$	V_y $t \in (t_2, t_3]$
$D^*_{RL} \le D^*_{SL} \le D^*_{TL}$	t_R	t_S	t_T	V_3	V_1
$D^*_{SL} \le D^*_{RL} \le D^*_{TL}$	t_S	t_R	t_T	V_5	V_1
$D^*_{SL} \le D^*_{TL} \le D^*_{RL}$	t_S	t_T	t_R	V_5	V_4
$D^*_{TL} \le D^*_{SL} \le D^*_{RL}$	t_T	t_S	t_R	V_6	V_4
$D^*_{TL} \le D^*_{RL} \le D^*_{SL}$	t_T	t_R	t_S	V_6	V_2
$D^*_{RL} \le D^*_{TL} \le D^*_{SL}$	t_R	t_T	t_S	V_3	V_2

TABLE II
DC VOLTAGE TERMS VERSUS VOLTAGE VECTOR

Voltage vector V_i	X_{V_iR}	X_{V_iS}	X_{V_iT}
$V_0 = [0, 0, 0]$	0	0	0
$V_1 = [0, 0, 1]$	-1	-1	2
$V_2 = [0, 1, 0]$	-1	2	-1
$V_3 = [0, 1, 1]$	-2	1	1
$V_4 = [1, 0, 0]$	2	-1	-1
$V_5 = [1, 0, 1]$	1	-2	1
$V_6 = [1, 1, 0]$	1	1	-2
$V_7 = [1, 1, 1]$	0	0	0

Sorting the estimated duties D^*_{kL} yields the active voltage vectors utilized for the switching cycle as shown in Table I.

The voltage applied to the inverter-side inductor for each phase can be found by forming Thévenin equivalent circuits [9]. The inductor current slopes can be calculated as follows:

$$\alpha_{V_i k}\ [n+1] = \frac{X_{V_i k} V^*_{\mathrm{DC}}\,[n]\,/3 - v^*_{kcn}\,[n]}{L_{ikL}\,[n]} - \frac{\Delta i^*_{ikL}\,[n+1]}{T_{sL}}$$

$$V_i = \{V_0, V_1, \ldots, V_7\}\,. \tag{3}$$

The dc voltage applied during each voltage vector for each phase can be calculated by substituting the dc voltage terms X_{Vk} into (3). DC voltage terms X_{Vk} derived for each phase using Thévenin equivalent circuits are tabulated in Table II.

For example, to calculate R-phase ripple $i_{iR.3\mathrm{W}}(t)$, if the relation between calculated duties is $\boldsymbol{D^*_{RL} \le D^*_{SL} \le D^*_{TL}}$, according to Table I, the two active vectors are $V_{xR} = V_{3R}$ and $V_{yR} = V_{1R}$. Now to calculate the R-phase ripple, the slopes $\alpha_{V_7 R},\ \alpha_{V_3 R},\ \alpha_{V_1 R},\ \mathrm{and}\alpha_{V_0 R}$ are calculated using (3) with the parameters obtained in Table II. $X_{V_7 R} = 0,\ \ X_{V_3 R} = -2,\ \ X_{V_1 R} = -1,\ \ \mathrm{and} X_{V_0 R} = 0$, and then substituted to (1).

B. 3P4W Inverter Side Inductance Current Ripple Model

3P4W inverter time-domain ripple model with only two voltage vectors is shown as follows:

$$i_{ik.4\mathrm{W}}\ (t) = \begin{cases} \alpha_{m.k}\left[n+1\right]\cdot\left(t-t_0\right), & t_0 \le t \le t_k \\ i_{ik4\mathrm{W}}\left(t_k\right)+\alpha_{d.k}\left[n+1\right]\left(t-t_k\right), & t_k < t \le \frac{T_{sL}}{2} \\ -i_{ik4\mathrm{W}}\left(T_{sL}-t\right), & \frac{T_{sL}}{2} < t \le T_{sL} \end{cases}. \quad (4)$$

where $t_0 = 0$ and the moment of switching between magnetization and demagnetization t_k is calculated as

$$t_k = \frac{T_{sL}\left(1-D^*_{kL}\left[n+1\right]\right)}{2} \quad (5)$$

where duty $D^*_{kL}[n+1]$ is the estimation of LFHPI duty ratio performed by HFLPI controller.

Magnetization $\alpha_{m.k}$ and demagnetization $\alpha_{d.k}$ slopes are calculated as

$$\alpha_{m.k}\ [n+1] = \frac{V^*_{\mathrm{DC}}\left[n\right]-v^*_{kcn}\left[n\right]}{L^*_{ikL}\left[n\right]} - \frac{\Delta i^*_{ikL}\left[n+1\right]}{T_{sL}}$$
$$\alpha_{d.k}\ [n+1] = \frac{-V^*_{\mathrm{DC}}\left[n\right]-v^*_{kcn}\left[n\right]}{L^*_{ikL}\left[n\right]} - \frac{\Delta i^*_{ikL}\left[n+1\right]}{T_{sL}}. \quad (6)$$

where the terms: $V^*_{\mathrm{DC}}[n]$, $v^*_{kcn}[n]$, $L^*_{ikH}[n]$, and $\Delta i^*_{ikL}[n+1]$ are all estimations of what is being sampled or calculated by the LFHPI controller. These estimations are obtained by the HFLPI controller either by synchronized sampling with LFHPI or predetermined. Sending sample data from one controller to the other would require fast and reliable connectivity. This is costly; thus, synchronized sampling is adopted.

General ripple models are defined for $t \in [0,\ T_{sL}]$. Using these models, the control system can calculate reference current for ripple attenuation. A sequence of λ equidistantly placed (in time) reference points is calculated. λ is called the frequency ratio in this work and is defined as

$$\lambda\ = \frac{fswH}{fswL}\ . \quad (7)$$

C. Connection Between 3P3W and 3P4W Ripple Models

Models of 3P3W and 3P4W ripples are interconnected. Elimination of the zero-sequence current from the 3P4W ripple allows us to calculate the 3P3W ripple. This connection can be expressed as follows:

$$i^*_{ik3\mathrm{W}}\ (\mathrm{t}) = i_{ik4\mathrm{W}}\ (\mathrm{t}) - \frac{\sum_k i_{ik4\mathrm{W}}\left(\mathrm{t}\right)}{3}. \quad (8)$$

Using this connection between models, the designer has an alternative way to calculate the 3P3W ripple.

D. Conditions for the HbFPIS to Achieve the Ripple Compensation

Unless the controllers are implemented on a single microcontroller, the control system requires synchronization of the PWM carriers. Synchronized carriers allow for coordination of the ripple attenuating reference sequences. If the next duty $D_{kL}[n+1]$ of LFHPI is unknown to HFLPI and is not communicated, then it has to be estimated. To form precise ripple attenuation, the following command set of conditions has to be met.

1) Inductor value $L_{ikL}[n]$, switching period T_{sL}, and the next current reference point $I_{\mathrm{ref}kL}[n+1]$ have to be known to the HFLPI controller.
2) Samples of the capacitor voltage $v_{kcn}[n]$, inductor current $i_{ikL}[n]$, and dc-side voltage $V_{\mathrm{DC}}[n]$ that are being sampled and used by LFHPI controller have to be estimated.
3) The modulation technique of LFHPI has to be known to HFLPI, so the ripple model matches reality.

The first condition can be met by knowing the parameters beforehand or setting them with the user interface. The second condition can be met by either sending the samples over a communication channel or synchronized sampling and computing of parameters.

The third condition is not discussed in this article, as the modulation technique is predetermined by the control law. In the next section, the method of synchronization without a dedicated communication channel will be discussed.

III. AUTOMATIC SYNCHRONIZATION BASED ON RIPPLE SIMULATION

Using current control, HFLPI forms the sequence of commands that delivers energy to the grid and compensates the LFHPI ripples. The coordination of operations linked to the controller carriers for synchronized and unsynchronized cases is shown in Fig. 2.

Carrier time discrepancies between controllers would appear due to factors like oscillator temperature shifts, crystal purity, etc. Even a small imperfection of the oscillator would affect the switching frequency ratio. Left unsynchronized over a long time would lead to sliding carriers, unsynchronized sampling, and ripple attenuation command misplaced.

One way to solve the synchronization issue is by using the wired synchronization. In the wired scheme, the LFHPI controller acts as a primary updating the carrier of the secondary HFLPI controller at every carrier crest. This way of synchronization, however, has several problems.

1) Parasitic parameters result in a propagation delay. The system would require manual adjustment.
2) The galvanic connection between two converters operating at hybrid frequencies may generate unwanted electromagnetic interference problems.
3) Primary–secondary architecture has preprogrammed roles in the modules. This reduces the reliability of modules.

Automatic synchronization of inverters without a dedicated wired channel would solve these problems. Moreover, modules would become more autonomous and reliable. The wireless synchronization technique will be discussed in the following subsection.

A. Time-Domain Cross-Correlation Ripple Matching-Based Synchronization Method

In the wired synchronization scheme, each switching cycle of the LFHPI carriers is synchronized. Primary controller LFHPI sends a synchronization pulse at every crest of the carrier. This, in turn, modifies the state of the secondary HFLPI controller. Synchronizing pulse resets and restarts the carriers of the HFLPI

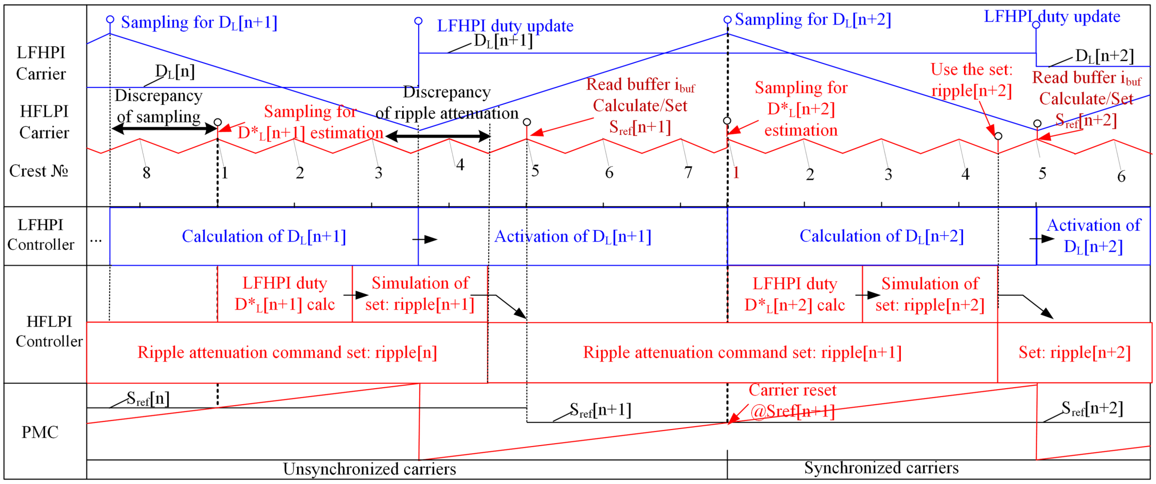

Fig. 2. Synchronization of the carriers of HFLPI and LFHPI.

controller and resets the ripple attenuation command sequence. In the proposed synchronization algorithm, the restart of the carrier and ripple command sequence is performed by the HFLPI controller itself. For this, the HFLPI controller estimates the duration of the LFHPI switching cycle by the period-measurement counter (PMC). HFLPI controller predetermines the switching period of LFHPI expressed in the oscillations of crystal T_{sHX} and the frequency ratio λ. PMC then counts from 0 up to $\lambda \cdot T_{sHX}$ to estimate the period of LFHPI. To adjust the reset moment, synchronization reference S_{ref} is introduced. PMC and S_{ref} are shown in Fig. 2. Each of the λ switching periods are enumerated in the microprogram. Switching period number counter is increased at every crest of HFLPI carrier. Match between S_{ref} and PMC defines the moment when HFLPI carrier and period number are reset. Finding the correct reference $S_{\text{ref}}[n+1]$ that would align the carriers is the task of the synchronization algorithm.

To perform this calculation, samples of the LFHPI ripple are stored and compared to the modeled ripple. Each of the models (1), (4), or (8) allows for calculating ripple with any given phase shift θ.

The phase shift θ is the initial timestamp recalculated in radians. Starting from initial timestamp $\lambda + 1$ of evenly distributed timestamps are calculated with the remainder function as follows:

$$t_\theta\ (k) = \left(\frac{\theta}{2\pi} T_{sL} + k \cdot T_{sH}\right)\ \text{mod}\ T_{sL}$$
$$k\ = \{0, 1, \ldots, \lambda\}\ ,\quad -\pi < \theta \leq \pi. \tag{9}$$

The remainder function wraps the timestamps around when $t > T_{sL}$ or $t < 0$. A set of timestamps (9) is used in (1), (4), or (8) to calculate discrete ripple at any shift. The resulting permutated ripple is stored as $i_{ik.t_\theta}$. The LFHPI ripple current is sampled at every crest of HFLPI controller carrier and stored in the buffer i_{buf}.

The metric of similarity or cross-correlation between measured ripple i_{buf} and modeled ripple $i_{ik.t_\theta}$ can be calculated as:

$$h\ (\theta) = \sum_{n}^{\lambda+1} i_{\text{buf}}\ [n] \cdot i_{ik.t_\theta}\ [n] \tag{10}$$

where $h(\theta)$ is the cross-correlation result depending on initial phase shift θ of the modeled ripple $i_{ik.t_\theta}$. Finding the phase shift θ that results in maximum similarity between model and measured ripple reveals the relative position of carriers.

LFHPI's ripple $i_{ikL}[n]$ is sampled and saved in a circular buffer i_{buf} of fixed size $\lambda + 1$. Stacking each sample of the inductor current forms a snapshot of the most recently measured inductor current ripple in the controller memory. Current samples $i_{ikL}[n]$ are saved either containing fundamental current or horizontal projection is calculated. Both ways are shown as

$$i_{\text{buf}} \leftarrow i_{ikL}\ [n]\ ,$$
$$\text{or}\ i_{\text{buf}} \leftarrow \left(i_{ikL}\ [n] - \frac{I_{\text{ref}kL}\ [n+1] - i_{ikL}\ [n]}{\lambda}\right). \tag{11}$$

Reading the buffer i_{buf} and synchronized sampling can be performed at any enumerated HFLPI crest, however, we will rigidly arrange these functions to the fixed crests.

For example, in the case shown in Fig. 2, the *crest №1* is bearing the function of synchronized sampling. In other words, measurements made at the *crest №1* are always used for the estimation of the duty. In the unsynchronized case, discrepancy between LFPHI sampling moment and HFLPI *crest №1* is presented as "discrepancy of sampling." This discrepancy leads to a worse estimation of LFHPI duty cycle. Moreover, the ripple attenuation sequence is misplaced which leads to worse ripple attenuation. The only appropriately placed ripple attenuation sequence in Fig. 2 according to the set "ripple[n+2]" appears after carrier reset. The carrier reset related to $S_{\text{ref}}[\text{n}+1]$ moves the HFLPI's *crest №1* and matches it with LFHPI sampling. In this design, the frame of buffered data contains the samples that were taken at {λ/2 + 1, …, λ, 1, …, λ/2 + 1} crests. For any even number λ>2, the first crest sample is placed in the middle of the buffer. Practically, with fixed size buffer, choosing the frame {λ/2+1, …, λ, 1, …, λ/2+1} means that the buffer reading is performed at the *crest № λ/2+1* (or *crest №5* in Fig. 2.).

To find the correct shift reference $S_{\text{ref}}[\mathrm{n}+1]$, the search algorithm has to be applied. Reaching the supremum of the metric (10), $\sup\limits_{\theta=(-\pi,\pi]} h(\theta)$ means that the samples in the buffer compared to the ripple model with the initial phase θ are matching. The search algorithm goal is to move the positions of crests in HFLPI by changing S_{ref} until the supremum of (10) is achieved for buffered ripple samples and ripple model at the desired phase θ_{ref}. In the example shown in Fig. 2 with *crest №1* chosen as synchronized sampling and crest №5 for buffer reading, the desired model phase should be $\theta_{\text{ref}} = 0$. This is because, at each LFHPI duty update, a new ripple is formed; thus, in the synchronized case, the buffer will contain the features of nonshifted ripple.

A primitive algorithm would be a brute force approach given as follows:

1) model ripple for a wide variety of shifts θ;
2) use metric (10) against measured samples;
3) find the θ_m that yields the maximum of the metric;
4) find error $\Delta\theta = \theta_m - \theta_{\text{ref}}$;
5) correct $S_{\text{ref}}[n+1]$ based on $\Delta\theta$.

Computationally, this is very expensive as it requires many instances of ripple modeling. Binary search and other $O(\log(n))$ algorithms can be used. But, the problem with these algorithms is that they still require calculating many instances of the ripple model calculation.

In a stable system, short misalignment of carriers does not bear catastrophic consequences and only reduces output current quality. So, the carriers can be synchronized gradually.

The algorithm of gradual synchronization

1) locally check whether the sampled ripple i_{buf} is matching the desired ripple model at θ_{ref} or one of two permutations generated by a slight shift right $\theta_{\text{ref}} + \delta\theta$ and left $\theta_{\text{ref}} - \delta\theta$ as

$$\begin{cases} h_l = h\left(\theta_{\text{ref}} - \Delta\theta\right) \\ h_m = h\left(\theta_{\text{ref}}\right) \\ h_r = h\left(\theta_{\text{ref}} + \Delta\theta\right). \end{cases} \tag{12}$$

2) Based on the relation between three cross-correlation results, the decision to the next reference phase shift is made as

$$S_{\text{ref}}\left[n+1\right] = \begin{cases} S_{\text{ref}}\left[n\right] - \delta S, h_l > h_m \geq h_r \\ S_{\text{ref}}\left[n\right] - \delta S, h_l > h_r \geq h_m \\ S_{\text{ref}}\left[n\right] + \delta S, h_r > h_m \geq h_l \\ S_{\text{ref}}\left[n\right] + \delta S, h_r > h_l \geq h_m \\ S_{\text{ref}}\left[n\right], h_m > h_l, h_r \end{cases} \tag{13}$$

where δS is the synchronization phase shift reference adjustment that can be chosen from the range

$$0 < \delta S \leq \frac{\delta\theta}{2\pi}\lambda T_{sHX} \tag{14}$$

where the expression λT_{sHX} is the PMC maximum value.

3) Algorithm is repeated and never terminated to prevent sliding carriers.

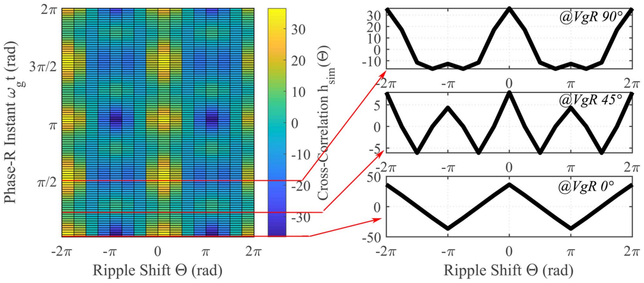

Fig. 3. Estimated search space λ = 8.

If the carrier's relative sliding is small, its effect on synchronization time can be omitted. The time to achieve synchronization varies from M to $(\lambda-1)M$ of LFHPI switching periods T_{sL}, which depends on adjustment size in (13): $\delta S = \frac{\delta\theta}{2\pi}\lambda T_{sHX}/M$ where $M \geq 1$.

For example, if $M = 1$, the maximum time to achieve the synchronization is $(\lambda-1)T_{sL}$ and the minimum time is T_{sL}. However, if the carrier's relative sliding speed is comparatively close to the synchronization phase shift reference adjustment applied per one switching period T_{sL}, there might be a case when the synchronization effort cannot keep up with the relative sliding of carriers. Either parameter *M* was chosen inappropriately big or the carrier's sliding is too rapid. This kind of rapid sliding cannot be caused by the crystal temperature shifts and is most probably due to coding error and would not be covered by the proposed algorithm.

The algorithm gradually reaches the state when samples in the buffer match the model calculated at θ_{ref}. In (13), this is the fifth state when $h_m > h_l, h_r$ and $S_{\text{ref}}[n+1]$ becomes static. However, the local search algorithm may bind to the local extrema. To check whether local extrema exist, an approximate search field is calculated. Cross-correlation is performed on modeled ripple against its own phase-shifted versions over one grid-cycle. Cross-correlation results are placed on the heat map as an approximate search space in Fig. 3.

Clear single supremum is only achieved when the grid is at $\omega_g t \approx 0, \pi$. In other cases, local extrema exist. Visualization of the search space reveals that local extremums always localized π radians away from the global one. Using this additional rule of synchronization, we define

$$S_{\text{ref}}\left[n+1\right] = \begin{cases} S_{\text{ref}}\left[n\right], & h_m \geq h_{ck} \\ S_{\text{ref}}\left[n\right] + \frac{\lambda \cdot T_{sHX}}{2}, & h_m < h_{ck} \end{cases} \tag{15}$$

where $h_{ck} = h(\theta_{\text{ref}} + \pi)$ is an additional cross-correlation requiring additional ripple model at $\theta_{\text{ref}} + \pi$.

Three phase-shifted model calculation instances are required for each step before supremum or extremum is reached. One additional instance would be required when the extremum is reached.

IV. DIRECT DIGITAL CONTROL FOR HBFPIS

This section provides the derivation of direct digital control for HF and LF modules. For grid-connected inverters, direct

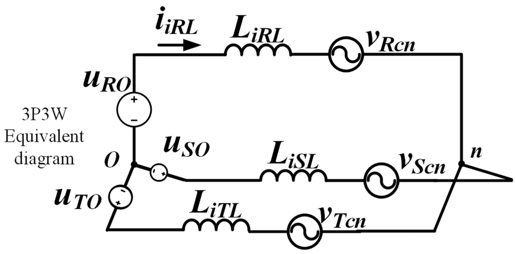

Fig. 4. Equivalent diagram of the 3P3W inverter.

digital control provides equations for controlling the current of the inverter-side inductor. The derivation is based on finding the relationship between the average trajectory of the controlled current and the control parameter. This process is often referred to as the division–summation (D–Σ) process. The duty cycle D_k of PWM is the control parameter in this control. For inverters with an *LC* filter, the control equations can be derived from the equivalent diagram provided in Fig. 4.

For 3P3W inverter, using Kirchhoff's voltage law (KVL) in the equivalent diagram in Fig. 4 yields

$$v_{nO} = u_{kO} - L_{ikL}\frac{di_{ikL}}{dt} - v_{kcn}. \tag{16}$$

The general expression of common mode voltage for each voltage vector can be derived using linear combination. For this nonzero terms, a_R, a_S, anda_T are introduced for any voltage vector V_j

$$v_{nO.Vj} = \frac{1}{\sum_{k=\{R,S,T\}} a_k}\left(\sum_{k=\{R,S,T\}} a_k u_{kO} - \sum_{k=\{R,S,T\}} a_k \frac{L_{ikL}di_{ikL}}{dt} - \sum_{k=\{R,S,T\}} a_k u_{kcn}\right). \tag{17}$$

In 3P3W, the approach is to find the average common-mode voltage over one switching cycle

$$\overline{v_{nO}} = \frac{T_0 v_{nO.V0} + T_x v_{nO.Vx} + T_y v_{nO.Vy} + T_7 v_{nO.V7}}{T_s} \tag{18}$$

where T_i are the switching-time intervals and $v_{nO.V_i}$ are the amplitudes of the applied voltage vectors V_i with vector numbers $i = \{0,1,\ldots,7\}$ and $x \neq y = \{1,2,\ldots,6\}$ is a subset of vector numbers excluding the zero and the seventh vector.

Time derivatives of the currents in (17) are represented with discretized form by replacing the intervals T_j as period T_s multiplied by duty ratios and di_i as a finite increment of current Δi_i. Substituting discretized results into (18) for any adjacent four voltage vectors will yield

$$\overline{v_{nO}} = \frac{V_{DC}\left(a_R D_R + a_S D_S + a_T D_T\right)}{a_R + a_S + a_T} - \frac{a_R L_{iR}\Delta i_{iR} + a_S L_{iS}\Delta i_{iS} + a_T L_{iT}\Delta i_{iT}}{\left(a_R + a_S + a_T\right)T_s} - \frac{a_R v_{Rcn} + a_S v_{Scn} + a_T v_{Tcn}}{a_R + a_S + a_T}. \tag{19}$$

The only possible set of independent solutions for D_R, D_S, and D_T is discretized and written as

$$D_k\left[n+1\right] = \frac{\overline{v_{nO}}}{V_{\mathrm{DC}}} + \frac{v_{kcn}\left[n+1\right]}{V_{\mathrm{DC}}\left[n\right]} + \frac{L_{ikL}\Delta i_{ik}\left[n+1\right]}{V_{\mathrm{DC}}\left[n\right]T_s} \tag{20}$$

where $n+1$ is the next switching cycle, and $\Delta i_{ik}[n+1]$ is the current variation which will be defined later. The term $\frac{\overline{v_{nO}}}{V_{\mathrm{DC}}}$ set as an arbitrary value and can be varied for zero-sequence injection. In this case, $\frac{\overline{v_{nO}}}{V_{\mathrm{DC}}} = \frac{1}{2}$. The control laws for 3P3W and 3P4W are identical, thus interoperable between topologies.

For LFHPI, the current variation is defined as

$$\Delta i_{ikL}\left[n+1\right] = I_{\mathrm{ref}kL}\left[n+1\right] - i_{ikL}\left[n\right]. \tag{21}$$

The term $I_{\mathrm{ref}kL}[n+1]$ is the current command reference term, calculated depending on the proportion of energy sharing between HFLPI and LFHPI.

For HFLPI, the current variation is defined as

$$\Delta i_{ikH}\left[n+1\right] = I_{\mathrm{ref}kH}\left[n+1\right] - i_{ikL}\left[n\right] - i_{rpk}\left[n+1\right] \tag{22}$$

where $I_{\mathrm{ref}kH}[n+1]$ is the term of the fundamental current command reflecting the proportion of energy that is shared by HFLPI, and $i_{rpk}[n+1]$ is a term of ripple attenuation. To calculate the current ripple term $i_{rpk}[n+1]$, readers can use the models derived in Section II.

According to the concept state of controllability [22], the 3P3W inverter has two uncontrollable parameters: $\sum_{k\,=\,R,S,T} i_{ikL}(t)$ and $\sum_{k\,=\,R,S,T} v_{kcn}(t)$. The sum of current ripple commands for three phases would always result in zero, meaning that performing such current commands is feasible in the 3P3W topology.

V. SWITCHING FREQUENCIES AND FILTER DESIGN

A. *Ripple Attenuation Ratio for 3P3W Inductor Current Ripples*

Filter design in HbFPIS starts by determining the switching frequencies of two inverters. For LFHPI, the switching frequency is chosen based on the characteristics of the switching device. High-power inverters using insulated-gate bipolar transistors (IGBTs) usually operate at frequencies below 10 kHz. For this work, the LFHPI operating frequency is chosen as 6.12 kHz. HFLPI frequency is chosen based on the ripple attenuation quality that depends on frequency ratio λ. For comparison purposes, ripples in 3P4W and 3P3W inverters are shown in Fig. 5.

In [6], the ripple attenuation ratio versus frequency ratio is presented in the closed-form expressions for 3P4W. Ripple attenuation ratio α is defined as a ratio between the rms of the attenuated output signal and the rms of the original signal. This

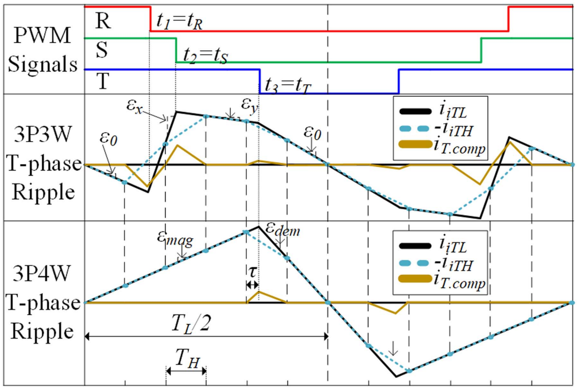

Fig. 5. 3P3W and 3P4W ripples canceled with the same frequency ratio.

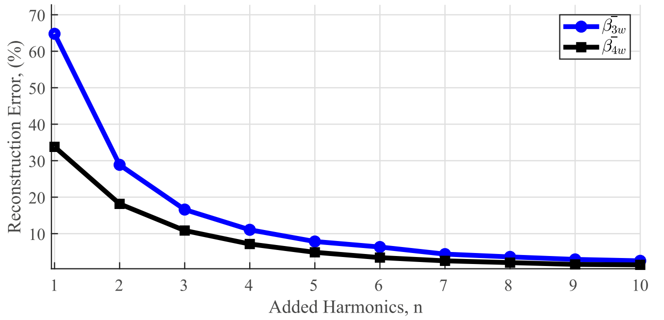

Fig. 6. Average error of reconstruction of ripple signal in 3P3W and 3P4W inverter side inductance.

parameter shows the quality of ripple attenuation. For 3P3W, an alternative way of analyzing the ripple attenuation is presented.

According to the Nyquist–Shannon sampling theorem

> "A function $f(t)$ containing no frequencies higher than F Hertz is completely re-constructable by sampling it at a series of timestamps spaced $\frac{1}{2F}$ seconds apart"

Looking at attenuation as a process of reconstruction of the time-limited function with limited samples is a time-domain approach. Instead, to gain some knowledge by comparing 3P3W ripple to 3P4W, let us compare the harmonic composition of two types of ripples. For this, let us represent (1) and (4) as a sum of harmonic functions using Fourier transformation

$$f_{FT}(t) = \frac{a_0}{2} + \sum_{m=1}^{\infty}\left(a_m\cos\left(\frac{2mt}{T_L}\right)+b_m\sin\left(\frac{2mt}{T_L}\right)\right). \tag{23}$$

Ripple is an odd, unbiased function, so terms $a_0 = 0$, $a_m = 0$, and b_m can be found as

$$b_m = \frac{4}{T_L}\int_0^{TL/2} f(t)\sin\left(\frac{2mt}{T_L}\right)dt. \tag{24}$$

Simple integration of (24) for functions (1) and (4) yields two amplitude terms $b_{3w}(m)$ and $b_{4w}(m)$. Limiting summation to the first n harmonic components, reconstruction of the original function in frequency-domain can be written as

$$\begin{cases} g_{3w}(t,n) = \sum_{m=1}^{n} b_{3w}(m)\sin\left(\frac{2mt}{T_L}\right) \\ g_{4w}(t,n) = \sum_{m=1}^{n} b_{4w}(m)\sin\left(\frac{2mt}{T_L}\right) \end{cases}. \tag{25}$$

The frequency-domain analogy of ripple reconstruction error ratio then can be written as

$$\begin{cases} \beta_{3w}(n) = \dfrac{\sqrt{\int_0^{\frac{TL}{2}} (i_{ik.3W}(t) - g_{3w}(t,n))^2 dt}}{\sqrt{\int_0^{\frac{TL}{2}} i_{ik.3W}(t)^2 dt}} \\ \beta_{4w}(n) = \dfrac{\sqrt{\int_0^{\frac{TL}{2}} (i_{ik.4W}(t) - g_{4w}(t,n))^2 dt}}{\sqrt{\int_0^{\frac{TL}{2}} i_{ik.4W}(t)^2 dt}} \end{cases}. \tag{26}$$

Ripple reconstruction error shows the quality of reconstruction depending on how many harmonic components are used for the reconstruction of the ripple. Using control law (20) for phase-R together with ripple models for 3P3W and 3P4W, the ripples are calculated at 0°, 15°, 30°, …, 90° of phase-R grid voltage instants. In both 3P3W and 3P4W, the same dc voltage, ac voltage, and inductance parameters are used. These ripples are reconstructed with varying amounts of harmonics n = 1,2,…,10. The reconstruction error ratio (26) is calculated for each ripple shape in 3P3W and 3P4W systems. The average errors of reconstruction $\overline{\beta_{3w}}$ and $\overline{\beta_{4w}}$ are shown in Fig. 6.

The reconstruction error of the 3P3W ripple is consistently higher than that of the 3P4W ripple. This indicates that the 3P3W ripple is harmonically more complex. Going back to the Nyquist–Shannon theorem: using λ (frequency ratio) samples would recover up to $\frac{\lambda}{2}$ subharmonics of the ripple signal. The 3P3W HbFPIS ripple attenuation would require an increased frequency ratio compared to the 3P4W HbFPIS to achieve the same attenuation. In this work, the frequency ratio $\lambda = 8$ is chosen, and the average reconstruction error for 3P3W, $n = 4$, is $\overline{\beta_{3w}} = 11\%$. The average reconstruction error is 3 times lower than the time domain ripple attenuation ratio for 3P4W ripple from [6]. Taking this scaling into account, in the worst case, it is expected to have a ripple attenuation ratio $11\% < \alpha_{3w} \leq 33\%$. With this alternative way to analyze ripple attenuation, the filter design can be continued.

B. Filter Design of 3P3W HbFPIS

The method of filter design partially follows [23]. The inductance for HFLPI is chosen taking into account dynamic response.

First, knowing the per phase apparent power $S_{\text{ph}} = \frac{S_{\text{tot}}}{3}$, where S_{tot} is the total apparent power of the inverter, grid voltage frequency f_g and phase voltage v_{gk}, for both 3P3W and 3P4W, and the capacitor are chosen by limiting the power factor variation ΔPF to some acceptable level

$$C_k = \Delta\text{PF}\cdot C_B = \frac{\Delta\text{PF}\cdot S_{\text{ph}}}{2\pi f_g v_{gk}^2}. \tag{27}$$

The grid-side harmonics are reduced passively by the grid-side inductor L_{gk}. The expected ripple attenuation ratio α and switching ripple reduction ratio on the grid side k_{ig} will determine the value of grid-side inductance as

$$L_{gk} = \frac{\frac{\alpha}{k_{ig}} + 1}{(2\pi f_{sL})^2 C_k}. \tag{28}$$

TABLE III
SYSTEM SPECIFICATIONS AND FILTER DESIGN

	Symbol	Description	Value
Specifications	$\boldsymbol{V_{DC}}$	DC bus voltage	760 V
	$\boldsymbol{S_{LF}}$	LFHPI power rating	16 kVA
	$\boldsymbol{S_{HF}}$	HPLFI power rating	4 kVA
	$\boldsymbol{v_g}$	Phase voltage of grid	220 V
	$\boldsymbol{f_g}$	Grid frequency	60 Hz
Requirements	$\boldsymbol{\Delta PF}$	Power factor variation	≤10 %
	$\boldsymbol{k_{ii}}$	Ratio of inverter side current maximum ripple per rated current	≤60 %
	$\boldsymbol{k_{ig}}$	Ratio of grid side current maximum ripple per rated current	≤15 %
Design Results	$\boldsymbol{f_{sL}}$	LFHPI frequency	6 kHz
	$\boldsymbol{f_{sH}}$	HFLPI frequency	48 kHz
	$\boldsymbol{C_k}$	AC filter capacitor	30 μF
	$\boldsymbol{L_{ikL.3W}@0A}$	LFHPI inductance	720 μH
	$\boldsymbol{L_{ikH.3W}@0A}$	HFLPI inductance	172 μH
	$\boldsymbol{L_{gk}\ (\alpha = 11-33\%, k_{ig} = 5\%)}$	Grid-side inductance	72 –171 μH
	$\boldsymbol{L_{gk}\ (\alpha = 100\%, k_{ig} = 5\%)}$	Grid-side inductance required without ripple attenuation	473 μH

In 3P3W, the inverter-side inductor experiences maximum current ripple at either grid voltage peaks or zero crossing. This is determined by the ratio between dc source and grid voltage.

Inverter-side inductance in the 3P3W inverter can be calculated as

$$L_{ikL.3\mathrm{W}} = \frac{V_L}{\Delta i_{ppkL.\max}} \Delta t$$
$$= \begin{cases} \frac{\left(\frac{2}{3}V_{\mathrm{DC}} - \sqrt{2}v_{gk}\right)}{\Delta i_{ppkL.\max}} \frac{3\sqrt{2}v_{gk}T_{sL}}{4V_{\mathrm{DC}}}\Big|_{\text{at } v_{gk}.pk}, & \frac{v_{gk}}{V_{\mathrm{DC}}} \leq \frac{1}{9}\left(3\sqrt{2} - \sqrt{6}\right) \\ \frac{\sqrt{6}v_{gk}T_{sL}}{6\Delta i_{ppkL.\max}}\Big|_{\text{at } v_{gk}.zc}, & \frac{v_{gk}}{V_{\mathrm{DC}}} > \frac{1}{9}\left(3\sqrt{2} - \sqrt{6}\right). \end{cases} \tag{29}$$

In the 3P3W topology, the ripple has a complicated structure of seven segments belonging to two active and two passive vectors. Simplified, two passive vectors are almost identical, so only three distinct vectors are applied over the switching cycle. There always exist two vectors codirected in terms of magnetization and one opposite. Ignoring the middle amplitude vector, the two most opposed magnetizing and demagnetizing vectors are arranged to attenuate each other. The inductance that would match the occurring slew rates in this arrangement for 3P3W HbFPIS, then can be calculated as

$$L_{ikH.3\mathrm{W}} = \frac{\sqrt{6}v_{gk}T_{sH}}{6\Delta i_{ppkH.\max}} \leq \left|\frac{\frac{1}{3}V_{\mathrm{DC}} - \frac{1}{2}|v_{Rcn}|_{\max}}{-\frac{1}{3}V_{\mathrm{DC}} - \frac{1}{2}|v_{Rcn}|_{\max}}\right| \cdot L_{ikL.3\mathrm{W}}. \tag{30}$$

Specifications and the set of filter parameters of HbFPIS designed exclusively for three-wire setting are shown in Table III. The stability analysis is presented in the next section.

VI. CURRENT TRACKING CAPABILITY AND STABILITY ANALYSIS OF 3P3W HBFPIS

The most appropriate way to analyze a digitally controlled system is in the z-domain using direct synthesis or Tustin's method. However, operation at different frequencies of two parallel inverters in HbFPIS forces us to analyze the system as a multi-rate system. Moreover, the plant has to be digitized to have all of the elements in the z-domain. However, it is not clear how to digitize a single plant controlled simultaneously by hybrid frequency controllers. This can be a topic for future research. A suitable way is to use the pseudocontinuous-time approach of system analysis [24]. The sampler, zero-order-hold (ZOH), and delays are approximated as continuous time blocks in the s-domain. First-order Pade approximation is used for the exponential representation of ZOH and delays.

A. Current Tracking Capability Analysis

A diagram reflecting the connection between the 3P3W plant and controllers is shown in Fig. 7. Blocks $G_{dL}(s)$ and $G_{dH}(s)$ are defined as the equivalent s-domain blocks of delays, sample-hold, and a sampler as follows:

$$G_{dL}(s) = \frac{1}{T_{sL}} \cdot e^{-y_L s T_{sL}} \cdot \frac{\left(1 - e^{-sT_{sL}}\right)}{s}$$
$$G_{dH}(s) = \frac{1}{T_{sH}} \cdot e^{-y_H s T_{sH}} \cdot \frac{\left(1 - e^{-sT_{sH}}\right)}{s} \tag{31}$$

where y_L and y_H are the delay constants falling within 0–1.5. The first-order Pade approximation of the exponent function is applied to (31). Inductance and capacitance values are constant, and time-domain signals v_{kgn} and V_{dc} are mapped to the s-domain as constants.

The transfer functions of inductor-side current and grid-side current in relation to reference current are derived as

$$G_{iiL} = \frac{i_{ikL}}{i_{\mathrm{ref}kL}}\Big|_{i_{\mathrm{ref}kH}=0} = \frac{B_{kL}/A_{kL}}{G_{denum}} \tag{32}$$

$$G_{iiH} = \frac{i_{ikH}}{i_{\mathrm{ref}kH}}\Big|_{i_{\mathrm{ref}kL}=0} = \frac{B_{kH}/A_{kH}}{G_{denum}} \tag{33}$$

$$G_{igL} = \frac{i_{gk}}{i_{\mathrm{ref}kL}}\Big|_{i_{\mathrm{ref}kH}=0} = \frac{G_{iiL}}{\Gamma_k}\left(1 + \frac{N_{kH}}{A_{kH}}\right) \tag{34}$$

$$G_{igH} = \frac{i_{gk}}{i_{\mathrm{ref}kH}}\Big|_{i_{\mathrm{ref}kL}=0} = \frac{G_{iiH}}{\Gamma_k}\left(1 + \frac{N_{kL}}{A_{kL}}\right) \tag{35}$$

where

$$G_{denum} = \left(1 - \frac{N_{kL}N_{kH}}{A_{kL}A_{kH}}\right) \tag{36}$$

$$A_{kL} = s^3 L_{ikL}\left(L_{lk} + L_{gk}\right)C_k + s^2 G_{dL} f_{sL} L_{ikL}\Big(L_{lk} + L_{gk}\Big)C_k + s\Big(L_{ikL} + L_{lk} + L_{gk} - \Big(L_{lk} + L_{gk}\Big)G_{dL}\Big) + G_{dL} f_{sL} L_{ikL} \tag{37}$$

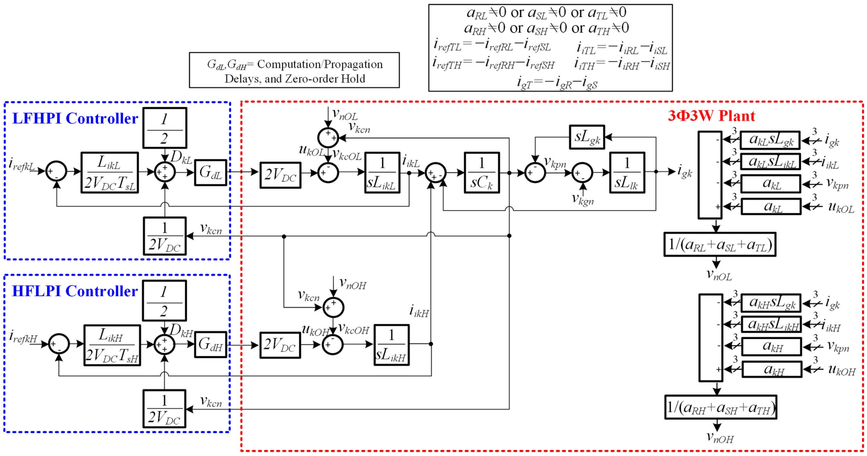

Fig. 7. Control block diagram of a 3P3W grid connected HbFPIS.

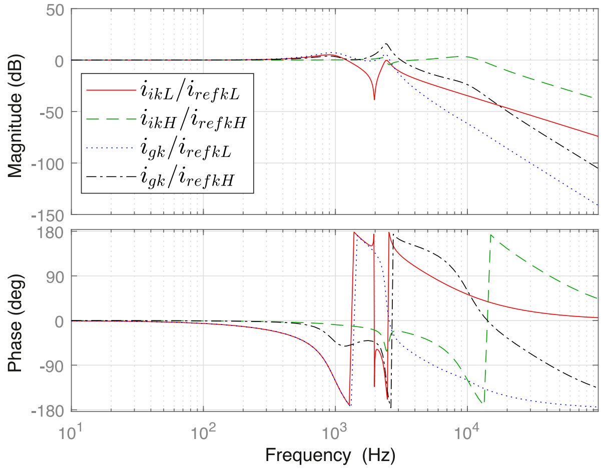

Fig. 8. Bode plots of (32)–(35) with the parameters as shown in Table III.

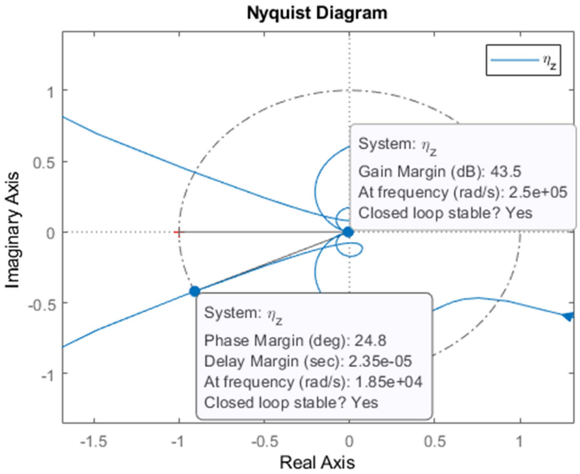

System: η_z
Gain Margin (dB): 43.5
At frequency (rad/s): 2.5e+05
Closed loop stable? Yes

System: η_z
Phase Margin (deg): 24.8
Delay Margin (sec): 2.35e-05
At frequency (rad/s): 1.85e+04
Closed loop stable? Yes

Fig. 9. Nyquist diagram of open loop representation of grid-connected parallel inverters $\eta_Z(\mathrm{s})$.

$$\begin{aligned} A_{kH} = {} & s^3\, L_{ikH}\left(L_{lk}+L_{gk}\right) C_k \\ & + s^2 G_{dH} f_{sH} L_{ikH}\left(L_{lk}+L_{gk}\right) C_k \\ & + s\left(L_{ikH}+L_{lk}+L_{gk}-\left(L_{lk}+L_{gk}\right) G_{dH}\right) \\ & + G_{dH} f_{sH} L_{ikH} \end{aligned} \tag{38}$$

$$B_{kL} = G_{dL} f_{sL} L_{ikL}\left(s^2\left(L_{lk}+L_{gk}\right) C_k+1\right) \tag{39}$$

$$B_{kH} = G_{dH} f_{sH} L_{ikH}\left(s^2\left(L_{lk}+L_{gk}\right) C_k+1\right) \tag{40}$$

$$\Gamma_k = s^2\left(L_{lk}+L_{gk}\right) C_k+1 \tag{41}$$

$$N_{kL} = s\left(L_{lk}+L_{gk}\right) G_{dL}-s\left(L_{lk}+L_{gk}\right) \tag{42}$$

$$N_{kH} = s\left(L_{lk}+L_{gk}\right) G_{dH}-s\left(L_{lk}+L_{gk}\right). \tag{43}$$

Bode plots of (32)–(35) are shown in Fig. 8. Magnitude of 0 dB at 60 Hz shows good tracking capability for the fundamental current command. Phase shift varies between $-0.4°$ and $-3.45°$. Considering that the ripple attenuation command is in the kHz range, digital preprocessing can be introduced. Preprocessing is used to cancel out the effects of delays and parasitic parameters of the plant in the kHz range. More about preprocessing applicable for digital control that is used for higher frequency signal generation is in [6].

Equivalent impedances of the grid, HFLPI, and LFHPI are derived as

$$Z_{gk} = \frac{2C_k R_{\mathrm{ESR}}\left(Lgk\ +\ Llk\right)s^2 +\ 2\left(Lgk+Llk\ \right)s}{s^2 C_k\ \left(Lgk\ +\ Llk\right)+sCk\ R_{\mathrm{ESR}}\ +\ 1} \tag{44}$$

$$Z_{OkL}\mid_{i_{\mathrm{refk}\,L}=\,0} = -\frac{v_{RTL}}{i_{iRL}} = \frac{3\left(s+G_{dL} f_L\right) L_{ikL}}{2\left(1-G_{dL}\right)} \tag{45}$$

$$Z_{OkH}\mid_{i_{\mathrm{refk}\,H}=\,0} = -\frac{v_{RTH}}{i_{iRH}} = \frac{3\left(s+G_{dH} f_H\right) L_{ikH}}{2\left(1-G_{dH}\right)}. \tag{46}$$

The Nyquist plot for impedance ratio η_Z never encircles -1, which means that the closed loop system representation of grid-connected parallel inverters $\frac{1}{1+\eta_Z(s)}$ is stable. Using a zoomed view in Fig. 9, the minimum phase margin of 24.8° at a frequency of 18.5 kHz can be found. A minimum gain margin of 43.5 dB

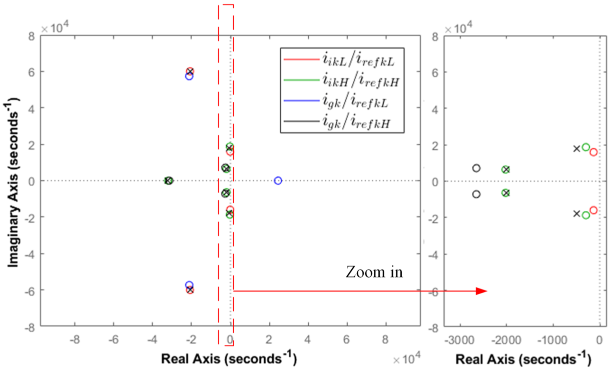

Fig. 10. Pole-zero plots of (32)–(35) transfer functions with the parameters as shown in Table III.

can be found at phase shift intersection of $-180°$ at 250 kHz. Both the phase and gain margins are sufficient.

B. Stability Analysis

Based on closed-loop transfer functions (32)–(35), the investigation of absolute stability is done. According to Fig. 10, all the poles remain in the left half-plane of the pole-zero plot. This implies that the system is stable; however, impedance-based stability analysis is performed to examine the margins of stability. According to [25], the system would be stable if the ratio of the grid impedance to the inverter parallel system output impedance seen at the connection point $\eta_Z = \frac{Z_{gk}}{Z_{OkL}||Z_{OkH}}$ satisfies the Nyquist criterion.

VII. SIMULATED AND EXPERIMENTAL RESULTS

The control law equation (20), 3P3W ripple model (1), Tables I and II, and wireless synchronization (9)–(15) are adopted for a 20-kW 3Φ3W grid-connected HbFPIS. The design and specifications used in simulations and laboratory tests are presented in Table III. The performance of current attenuation and wireless synchronization are investigated in simulations and experiments.

A. Simulated Results

Simulation results for 20-kW 3P3W grid-connected HbFPIS are presented in Figs. 11 and 12. The nonideal frequency ratio λ is set by slightly altering the switching frequency of LFHPI. The switching frequency of HFLPI is fixed. In a simulation, the nonideal frequency ratio is set as $\lambda = 8.0065$. The wireless synchronization algorithm is active to avoid carriers' slides. In Fig. 11(a), total harmonic distortions (THDs) of the output grid currents are 1.47%, 1.46%, and 1.48% for R-, S-, and T-phase currents, respectively. THDs of capacitor voltages are 0.6% for all three phases. To observe the attenuation, the inverter-side currents are collected as shown in Fig. 11(b).

The capability of the synchronization algorithm to wirelessly synchronize carriers is observed in Fig. 12. For this output signals C_L and C_H are introduced. The signal C_L belongs to the LFHPI and it is negated at every crest of the carrier. C_H belongs to HFLPI and it is negated at $S_{\text{ref}}[n]$ and PMC comparison match.

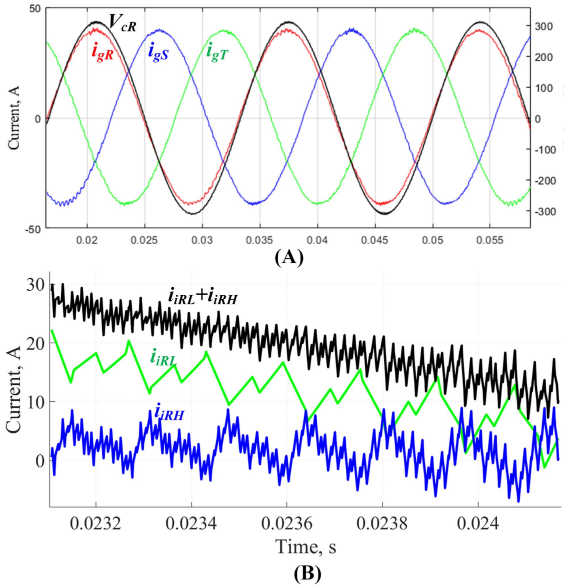

Fig. 11. Simulation of (a) grid voltage and currents and (b) LFHPI and HFLPI inverter side inductor currents.

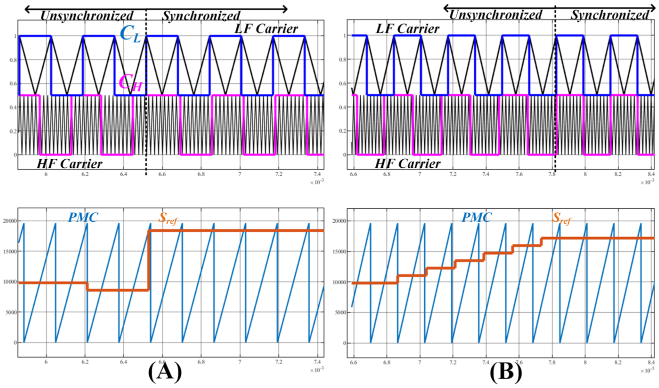

Fig. 12. Transient of initial synchronization when (a) local extremum of the metric is approached and (b) gradual synchronization is performed.

Two types of transient behavior are shown. For this HbFPIS synchronization algorithm starts working when the carriers are unsynchronized. In Fig. 12(a), the HFLPI uses a case (15) and immediately synchronizes. In Fig. 12(b), the HFLPI gradually synchronizes with a set of rules (13).

To check for harsher switching frequency misalignments, it is set to $\lambda = 7.974$ and up to $\lambda = 8.052$. HFLPI still preserves the ability to attenuate ripples if the wireless synchronization is active. The quality of the output current would slightly suffer, even though the carriers are still synchronized. For ratio $\lambda = 7.974$, the THDs of the output currents are 2.48%, 2.49%, and 2.46% for R-, S-, and T-phase currents, respectively. For ratio $\lambda = 8.052$, 2.13%, 2.05%, and 1.90% are obtained. The simulated conditions far exceed the typical deviations of the crystal [15].

B. Grid Connected Mode Experimental Results

The structure of the experimental setup is shown in the diagram of Fig. 13. Although the premise of wireless carrier

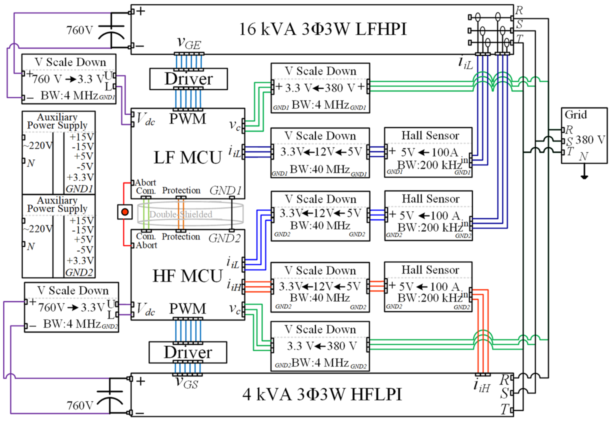

Fig. 13. Structural diagram of experimental setup.

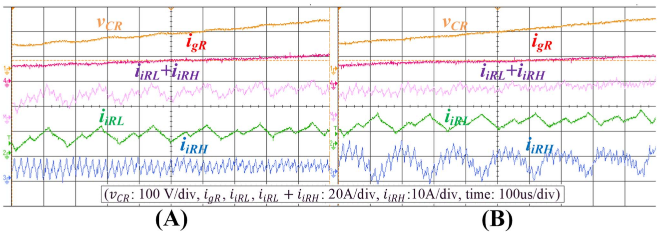

Fig. 14. Measured LFHPI and HFLPI inverter side inductor currents and their sum (a) without and (b) with ripple attenuation.

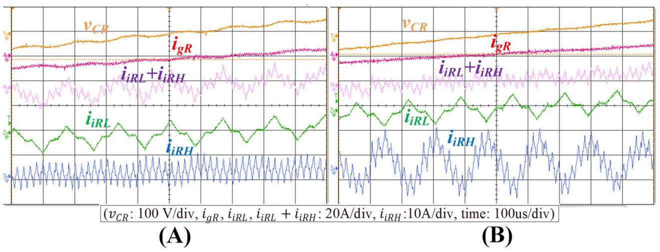

Fig. 15. Measured LFHPI and HFLPI inverter side inductor currents and their sum (a) without and (b) with ripple attenuation.

synchronization is to increase the autonomy of HbFPIS modules wirelessly, in this experimental set, some wired communication still exists. Handshake and protection signals are sent in a wired fashion; however, the carrier synchronization is done autonomously by HFLPI itself. The HFLPI module has an additional current sensor based on the Hall effect. This sensor is magnetically connected to the LFHPI to measure the inductance current ripple. To be able to save ripple features, high unity bandwidth operational amplifiers are used for scaling down the signal, whereas the Hall sensor has a bottleneck bandwidth of 200 kHz. Both controllers employ a 12-bit successive approximation A/D converter with a conversion time of 0.48 μs per channel with a 60 MHz clock rate.

The experimental results of a 20-kW 3P3W Grid Connected HbFPIS are shown in Figs. 14–17. For comparison, the inverter sends power without and with ripple attenuation. Figs. 14 and 15 show measured attenuation of different shapes of the LFHPI

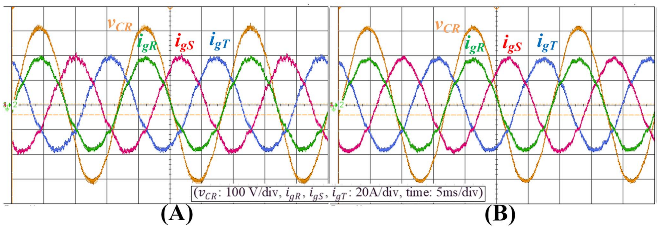

Fig. 16. Measured grid currents and capacitor voltage (a) without (iTHD = 5.78%) and (b) with (iTHD = 4.27%) ripple compensation.

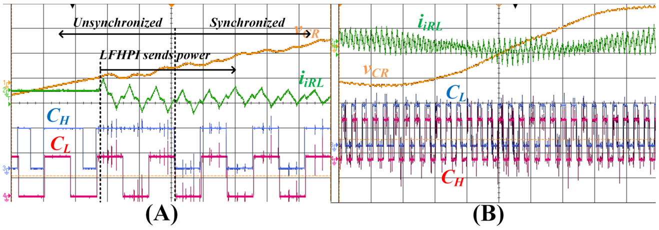

Fig. 17. (a) Transient of initial synchronization. (b) Persistent synchronization over half line-cycle.

ripple. The ripple generated by LFHPI in the sum of inverter-side inductor currents decreased from 12.15% to 7.93%, of the fundamental. In turn, this is also improving output currents as it is presented in Fig. 16.

C. Wireless Synchronization Experimental Results

The experimental results for the wireless synchronization algorithm are shown in Fig. 17. C_L reverses the state at every crest of the LFHPI carrier. To identify the synchronization, C_H reverses state at every first crest (or state reset) in HFLPI.

As can be observed, the two carriers are initially unsynchronized. C_H is sporadically changing until LFHPI starts to send power. After LFHPI sends current, the carriers are synchronized as shown in Fig. 17(a), and kept synchronized for the operation time as shown in Fig. 17(b). Transient in this case was similar to the one shown in Fig. 12(a), or immediate synchronization using the rule of synchronization (15). The synchronization in this example takes 3 T_{sL}= 0.49 ms. With gradual synchronization, it can take up to 7 T_{sL}= 1.1ms after the synchronization algorithm is activated to synchronize the carriers.

VIII. CONCLUSION

In this article, a new grid-connected 3P3W HbFPIS topology has been discussed. Digital control, ripple model, and additional use of models for wireless synchronization are presented. Compensation of inverter-side current ripple and wireless synchronization are both verified in the test with 20-kW grid-connected HbFPIS. The wireless carrier synchronization algorithm in general can be used in other systems with hybrid frequency using the same concept of extracting information from energy measurement channels. This can extend the autonomy and reliability of power modules. Differences in design and stability analysis between 3P4W and 3P3W HbFPIS are addressed, and expressions are presented for designers. The experimental 20-kW system can achieve an output current THDs $< 5\%$, complying with the IEEE-519 regulation.

REFERENCES

[1] J. Xu, S. Xie, and J. Kan, "LCL-filter design for grid-connected inverter to suppress grid-induced low-order current harmonics," in *Proc. IEEE Energy Convers. Congr. Expo.*, 2015, pp. 1178–1183, doi: 10.1109/ECCE.2015.7309824.

[2] X. Yu and A. M. Khambadkone, "Reliability analysis and cost optimization of parallel-inverter system," *IEEE Trans. Ind. Electron.*, vol. 59, no. 10, pp. 3881–3889, Oct. 2012, doi: 10.1109/TIE.2011.2175670.

[3] S. Xu, W. Cao, K. Liu, S. Wang, and J. Zhao, "Analysis and control of switching circulating currents in multi-module parallel SPWM converters," *IEEE Access*, vol. 6, pp. 32637–32648, 2018, doi: 10.1109/ACCESS.2018.2839757.

[4] C. Zhang, X. Yuan, J. Wang, W. Chen, B. Hu, and Z. J. Shen, "Adaptive power sharing and switching frequency control for power loss optimization in WBG/Si hybrid half-bridge converters," *IEEE Trans. Power Electron.*, vol. 38, no. 4, pp. 4440–4450, Apr. 2023, doi: 10.1109/TPEL.2022.3230747.

[5] T.-F. Wu, Y.-H. Huang, S. Temir, and C.-C. Chan, "3Φ4W hybrid frequency parallel uninterruptable power supply for reducing voltage distortion and improving dynamic response," *IEEE J. Emerg. Sel. Topics Power Electron.*, vol. 10, no. 1, pp. 906–918, Feb. 2022, doi: 10.1109/JESTPE.2021.3099061.

[6] T.-F. Wu, Y.-H. Huang, and Y.-T. Liu, "3Φ4W grid-connected hybrid-frequency parallel inverter system with ripple compensation to achieve fast response and low current distortion," *IEEE Trans. Ind. Electron.*, vol. 68, no. 11, pp. 10890–10901, Nov. 2021.

[7] C. Zhang et al., "WBG and Si hybrid half-bridge power processing toward optimal efficiency, power quality, and cost tradeoff," *IEEE Trans. Power Electron.*, vol. 37, no. 6, pp. 6844–6856, Jun. 2022, doi: 10.1109/TPEL.2021.3138464.

[8] C. Zhang, X. Yuan, J. Wang, B. Hu, X. Yin, and Z. J. Shen, "Optimization of power sharing and switching frequency in Si/WBG hybrid half-bridge converters using power loss models," *IEEE J. Emerg. Sel. Topics Power Electron.*, vol. 11, no. 3, pp. 2837–2849, Jun. 2023, doi: 10.1109/JESTPE.2022.3226196.

[9] T.-F. Wu, T. Sakavov, and Y.-H. Huang, "Current ripple compensation algorithm for paralleled three-phase three-wire hybrid frequency inverter systems," in *Proc. IEEE 12th Int. Symp. Power Electron. Distrib. Gener. Syst.*, 2021, pp. 1–5, doi: 10.1109/PEDG51384.2021.9494261.

[10] D. Jiang and F. Wang, "Current-ripple prediction for three-phase PWM converters," *IEEE Trans. Ind. Appl.*, vol. 50, no. 1, pp. 531–538, Jan./Feb. 2014, doi: 10.1109/TIA.2013.2270224.

[11] Q. Li, D. Jiang, and Y. Zhang, "Analysis and calculation of current ripple considering inductance saturation and its application to variable switching frequency PWM," *IEEE Trans. Power Electron.*, vol. 34, no. 12, pp. 12262–12273, Dec. 2019, doi: 10.1109/TPEL.2019.2903884.

[12] X. Pei, W. Zhou, and Y. Kang, "Analysis and calculation of dc-link current and voltage ripples for three-phase inverter with unbalanced load," *IEEE Trans. Power Electron.*, vol. 30, no. 10, pp. 5401–5412, Oct. 2015, doi: 10.1109/TPEL.2014.2375353.

[13] D. Jiang and F. Wang, "Variable switching frequency PWM for three-phase converters based on current ripple prediction," *IEEE Trans. Power Electron.*, vol. 28, no. 11, pp. 4951–4961, Nov. 2013, doi: 10.1109/TPEL.2013.2240701.

[14] B. B. Johnson, S. V. Dhople, A. O. Hamadeh, and P. T. Krein, "Synchronization of parallel single-phase inverters with virtual oscillator control," *IEEE Trans. Power Electron.*, vol. 29, no. 11, pp. 6124–6138, Nov. 2014, doi: 10.1109/TPEL.2013.2296292.

[15] M. Sinha, F. Dörfler, B. B. Johnson, and S. V. Dhople, "Synchronization of Liénard-type oscillators in uniform electrical networks," in *Proc. Amer. Control Conf.*, 2016, pp. 4311–4316, doi: 10.1109/ACC.2016.7525600.

[16] T. Xu and F. Gao, "Global synchronous pulse width modulation of distributed inverters," *IEEE Trans. Power Electron.*, vol. 31, no. 9, pp. 6237–6253, Sep. 2016, doi: 10.1109/TPEL.2015.2504361.

[17] K. Acharya, S. K. Mazumder, and M. Tahir, "A Wireless-communication based circulating-current controller for parallel three-phase inverters," in *Proc. IEEE 23rd Workshop Control Model. Power Electron.*, 2022, pp. 1–8, doi: 10.1109/COMPEL53829.2022.9830029.

[18] S. K. Mazumder, K. Acharya, and M. Tahir, "Wireless" control of spatially distributed power electronics," in *Proc. 20th Annu. IEEE Appl. Power Electron. Conf. Expo.*, 2005, vol. 1, pp. 75–81, doi: 10.1109/APEC.2005.1452889.

[19] E. Heiberg, T. Ebbers, L. Wigstrom, and M. Karlsson, "Three-dimensional flow characterization using vector pattern matching," *IEEE Trans. Vis. Comput. Graph.*, vol. 9, no. 3, pp. 313–319, Jul./Sep. 2003, doi: 10.1109/TVCG.2003.1207439.

[20] A. Amir, A. Levy, and L. Reuveni, "The practical efficiency of convolutions in pattern matching algorithms," *Fundamenta Informaticae*, vol. 84, no. 1, pp. 1–15, 2008.

[21] K. O'Shea and R. Nash, "An introduction to convolutional neural networks," 2015, *arXiv:1511.08458*.

[22] X. Li, L. Qu, W. Ren, C. Zhang, and S. Liu, "Controllability of the three-phase inverters based on switched linear system model," in *Proc. IEEE Int. Conf. Ind. Technol.*, 2016, pp. 287–292, doi: 10.1109/ICIT.2016.7474766.

[23] A. Reznik, M. G. Simões, A. Al-Durra, and S. M. Muyeen, "LCL filter design and performance analysis for grid-interconnected systems," *IEEE Trans. Ind. Appl.*, vol. 50, no. 2, pp. 1225–1232, Mar./Apr. 2014, doi: 10.1109/TIA.2013.2274612.

[24] C. H. Houpis, S. N. Sheldon, and J. J. D'Azzo, *Linear Control System Analysis and Design with MATLAB*, 5th ed. New York, NY, USA: Marcel Decker, Inc.

[25] J. Sun, "Impedance-based stability criterion for grid-connected inverters," *IEEE Trans. Power Electron.*, vol. 26, no. 11, pp. 3075–3078, Nov. 2011, doi: 10.1109/TPEL.2011.2136439.

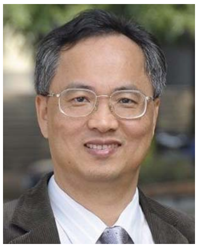

Tsai-Fu Wu (Senior Member, IEEE) received the Ph.D. degree in electrical engineering and computer science from the University of Illinois, Chicago, IL, USA, in 1992.

He is currently a Distinguished Professor with the Department of Electrical Engineering, National Tsing Hua University, Hsinchu, Taiwan. His research interests include the development of direct digital control for three-phase converters and the design of resonant converters for plasma applications.

Temir Sakavov (Member, IEEE) received the B.S. and M.S. degrees in electrical engineering from the Department of Electronic Engineering, Tomsk State University of Control Systems and Radioelectronics, Tomsk, Russia, in 2016 and 2018, respectively. He is currently working toward the Ph.D. degree in electrical engineering with the Department of Electrical Engineering, National Tsing Hua University, Hsinchu, Taiwan.

His current research focuses on hybrid-frequency parallel grid-connected inverters.

Chien-Chih Hung (Graduate Student Member, IEEE) received the M.S. degree in electronic engineering from Feng Chia University, Taichung, Taiwan, in 2016. He is currently working toward the Ph.D. degree in electrical engineering with the Department of Electrical Engineering, National Tsing Hua University, Hsinchu, Taiwan.

His current research focuses on switched-mode power supplies.

Jui-Yang Chiu (Graduate Student Member, IEEE) received the M.S. degree in electrical engineering from the National Chung Cheng University, Chiayi, Taiwan, in 2002. He is currently working toward the Ph.D. degree in electrical engineering with the Department of Electrical Engineering, National Tsing Hua University, Hsinchu, Taiwan.

Since 2002, he has been with the AcBel Polytech Inc., New Taipei City, Taiwan. His research interests include structure design and control of high-power converters and design of high-power inverters for electric vehicles.